AIP Applied Physics Letters

Predicting effective magnetoelectric response in magnetic-ferroelectric composites via phase-field modeling

T. N. Yang, Jia-Mian Hu, C. W. Nan, and L. Q. Chen

Citation: Applied Physics Letters **104**, 052904 (2014); doi: 10.1063/1.4863941
View online: http://dx.doi.org/10.1063/1.4863941
View Table of Contents: http://scitation.aip.org/content/aip/journal/apl/104/5?ver=pdfcov
Published by the AIP Publishing

Predicting effective magnetoelectric response in magnetic-ferroelectric composites via phase-field modeling

T. N. Yang,[1,a)] Jia-Mian Hu,[1,2] C. W. Nan,[2] and L. Q. Chen[1]
[1]*Department of Materials Science and Engineering, Pennsylvania State University, University Park, Pennsylvania 16802, USA*
[2]*State Key Laboratory of New Ceramics and Fine Processing, School of Materials Science and Engineering, Tsinghua University, Beijing 100084, China*

(Received 23 October 2013; accepted 19 January 2014; published online 3 February 2014)

A phase-field model coupled with constitutive equations is formulated to investigate the magnetoelectric cross-coupling in magnetic-ferroelectric composites. The model allows us to obtain equilibrium piezoelectric, piezomagnetic, dielectric, and magnetoelectric properties under a given magnetic or electric field, from the local distributions of polarization, magnetization, and strain in the composites. As an example, effective magnetoelectric coupling coefficient, i.e., magnetic-field-induced voltage output (or changes in polarization), of the $CoFe_2O_4$-$BaTiO_3$ composites is numerically calculated. Influences of the phase connectivity and the phase fraction of the composites on the magnetoelectric coupling coefficient are discussed. © *2014 AIP Publishing LLC*. [http://dx.doi.org/10.1063/1.4863941]

Magnetoelectric (ME) composites of magnetic and ferroelectric materials offer advantages over most single-phase ME materials due to their strong ME coupling effect at room temperature and great design flexibility.[1–5] The ME effect in such composites is normally understood as a product property of piezoelectricity in ferroelectrics and piezomagnetism in magnets,[6] leading to an electric polarization excited by a weak ac magnetic field (with either low or high frequencies) oscillating in a dc bias magnetic field, i.e., the direct ME effect, or conversely, a modulation of magnetization upon dc or ac electric fields. Among them, the direct ME effect has been extensively studied in various ME composites since the early 1970s[1] and can be potentially used to develop highly sensitive magnetic field sensors,[7–9] electric current probes,[10] novel ME read heads,[11] and energy harvesters.[12]

Theoretical approaches for such direct ME effect include the early parallel-series type model,[13] the Green's function technique (multiple-scattering approach),[6,14,15] micromechanical models[16–18] and the Landau–Ginzburg–Devonshire thermodynamic theory.[19–23] Although powerful, these continuum media methods are not capable of describing the spatial distribution of electric polarization, magnetization, and elastic fields upon applying an external magnetic field. Such mesoscopic insights, however, can provide more explicit guidelines for the improvement of the overall ME responses based on a deeper understanding of the microstructure-property correlation.

In this Letter, based on a phase-field model[24–31] coupled with constitutive equations, we can simulate both the effective ME coupling coefficients and the local distributions of electric polarization (i.e., ferroelectric domains) for bulk ME composites with magnetic inclusions in a ferroelectric matrix. The obtained ME coefficients are compared with existing results calculated by the Green's function approach.[6] Influences of several parameters including the phase fraction and aspect ratio of the magnetic inclusions on the ME coefficient were investigated.

Let us consider a typical two-phase bulk ME composite with periodically aligned cuboid-shaped $CoFe_2O_4$ (CFO) inclusions embedded in a $BaTiO_3$ (BTO) matrix, as shown in Fig. 1. In particular, by changing the aspect ratio $r = c/a$ of the CFO cuboids, the 2-2 type laminate ($r < 0.05$), 0-3 type ($0.05 \leq r < 10$) particulate, and 1-3 type ($r \geq 10$) rod ME composites can be described,[6] where each number denotes the connectivity of each phase,[32] as illustrated in Figs. 1(b)–1(d), respectively.

As an example, uniform spontaneous magnetization M_s and polarization P_s (magnetic and ferroelectric single-domains) along the out-of-plane axis are assumed for the CFO and BTO phases, respectively. Therefore, it is expected that it exhibits longitudinal magnetoelectric effect[6] based on the cross-product of the piezomagnetic and piezoelectric effects. In this case, relations between the stress $\boldsymbol{\sigma}$, strain $\boldsymbol{\varepsilon}$, electric displacement $\mathbf{D}$, electric field $\mathbf{E}$, magnetic induction $\mathbf{B}$, and magnetic field $\mathbf{H}$ can be described by the following linear constitutive equations,[6] i.e.:

$$\begin{cases} \boldsymbol{\sigma} = {}^{m}\mathbf{c}\boldsymbol{\varepsilon} - {}^{m}\mathbf{q}^{T}\mathbf{H} \\ \mathbf{D} = \kappa_0 {}^{m}\boldsymbol{\kappa}_r\mathbf{E} \\ \mathbf{B} = {}^{m}\mathbf{q}\boldsymbol{\varepsilon} + \mu_0 {}^{m}\boldsymbol{\mu}_r\mathbf{H}, \end{cases} \tag{1}$$

and

$$\begin{cases} \boldsymbol{\sigma} = {}^{e}\mathbf{c}\boldsymbol{\varepsilon} - {}^{e}\mathbf{e}^{T}\mathbf{E} \\ \mathbf{D} = {}^{e}\mathbf{e}\boldsymbol{\varepsilon} + \kappa_0 {}^{e}\boldsymbol{\kappa}_r\mathbf{E}, \\ \mathbf{B} = \mu_0 {}^{e}\boldsymbol{\mu}_r\mathbf{H} \end{cases} \tag{2}$$

for the CFO and BTO phases, respectively. Here, $\mathbf{c}$, κ_0, $\boldsymbol{\kappa}_r$, μ_0, and $\boldsymbol{\mu}_r$ denote the elastic stiffness, dielectric permittivity of vacuum, relative dielectric permittivity, magnetic permeability of vacuum, and relative magnetic permeability,

[a)]Author to whom correspondence should be addressed. Electronic mail: tuy123@psu.edu

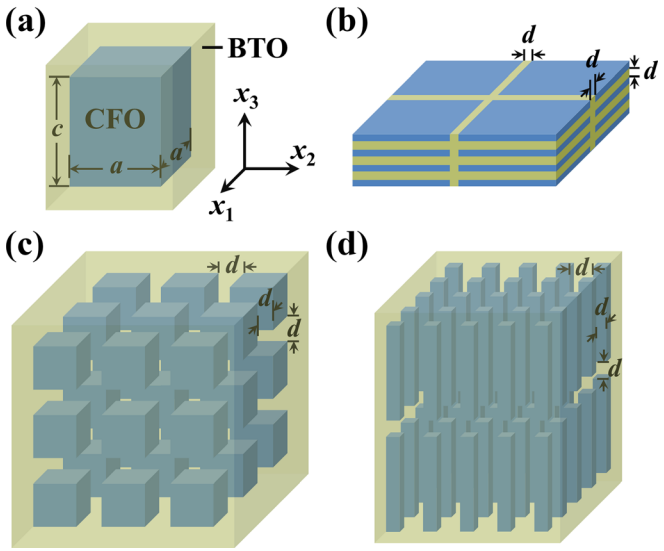

FIG. 1. (a) Schematic illustration of the chosen simulation zone of the phase-field model, where a cuboid CFO inclusion with a dimension of $a \times a \times c$ is embedded in a BTO matrix. The composite is described by periodically aligning CFO particles with a uniform separation distance d within all three directions. Composites of different phase connectivities including (b) 2-2, (c) 0-3, and (d) 1-3 types are obtained by varying the aspect ratios $r = c/a$ of the CFO inclusions. The CFO and BTO phases are assumed to be intimately contacted at their interface region, with no gas phase (porosity) incorporated in the model.

respectively. $\mathbf{e}$ and $\mathbf{q}$ are the piezoelectric and piezomagnetic coefficient tensors, respectively. The superscript T denotes the transpose of a tensor matrix, while presuperscripts m and e denote the constants of CFO (magnetic) and BTO (ferroelectric) phases, respectively. The room-temperature ($T = 298$ K) material constants are listed in Refs. 33–36.

The direct ME coupling coefficient in ME composites can be extracted from the linear field-dependence under a relatively small applied magnetic field,[3] i.e.,

$$\begin{cases} \boldsymbol{\sigma} = \mathbf{c}\boldsymbol{\varepsilon} - \mathbf{e}^T\mathbf{E} - \mathbf{q}^T\mathbf{H} \\ \mathbf{D} = \mathbf{e}\boldsymbol{\varepsilon} + \kappa_0\boldsymbol{\kappa}_r\mathbf{E} + \boldsymbol{\alpha}\mathbf{H} \\ \mathbf{B} = \mathbf{q}\boldsymbol{\varepsilon} + \boldsymbol{\alpha}^T\mathbf{E} + \mu_0\boldsymbol{\mu}_r\mathbf{H}. \end{cases} \tag{3}$$

Note that the magnetoelectric coefficient tensor $\boldsymbol{\alpha}$ in Eq. (3) is absent in both the magnetic and ferroelectric phases (Eqs. (1) and (2)).

The microstructure (i.e., magnetic/ferroelectric domains, phase distribution) of the bulk ME composite can be conveniently described within the framework of the phase-field model. Three non-conserved order parameters are utilized, including a local magnetization field $\mathbf{M}(\mathbf{x}) = (M_1, M_2, M_3)$, a local polarization field $\mathbf{P}(\mathbf{x}) = (P_1, P_2, P_3)$, and a phase order parameter $\eta(\mathbf{x})$ which describes the spatial distribution of the two phases, with $\eta(\mathbf{x}) = 1$ for the CFO phase and $\eta(\mathbf{x}) = 0$ for the BTO phase; $\mathbf{x}$ is the position vector herein. Furthermore, temporal evolution of both the local magnetization and polarization distributions can be described by the Allen–Cahn equation,[37] i.e.,

$$\begin{cases} \dfrac{\partial \mathbf{P}}{\partial t} = -L_1 \dfrac{\partial f}{\partial \mathbf{P}} \\ \dfrac{\partial \mathbf{M}}{\partial t} = -L_2 \dfrac{\partial f}{\partial \mathbf{M}}, \end{cases} \tag{4}$$

where L_1 and L_2 are kinetic coefficients related to evolution dynamics, and f is the local free energy density. Particularly, the formulation of the free energy density f in the present work is constructed based on previous phase-field models,[25,28] such that by minimizing it following Eq. (4), the constitutive equations, Eqs. (1) and (2), could be automatically satisfied. The total free energy is given by

$$f = f_{\text{magnetic}} + f_{\text{electric}} + f_{\text{elastic}}, \tag{5}$$

where f_{magnetic}, f_{electric}, and f_{elastic} are the magnetic, electric, and elastic energy, respectively, expressed as

$$\begin{aligned} f_{\text{magnetic}} = {} & \eta\left(\frac{\mu_0}{2({}^m\mu^\sigma_{rii} - 1)}M_i^2\right) \\ & + (1-\eta)\left(\frac{\mu_0}{2({}^e\mu_{rii} - 1)}M_i^2\right) \\ & - \frac{1}{2}\mu_0 H_i^d M_i - \mu_0 H_i^{\text{ext}} M_i, \end{aligned} \tag{6}$$

$$\begin{aligned} f_{\text{electric}} = {} & \eta\left(\frac{1}{2\kappa_0({}^m\kappa_{rii} - 1)}P_i^2\right) \\ & + (1-\eta)\left(\frac{1}{2\kappa_0({}^e\kappa^\sigma_{rii} - 1)}P_i^2\right) - \frac{1}{2}E_i^d P_i - E_i^{\text{ext}} P_i, \end{aligned} \tag{7}$$

$$\begin{aligned} f_{\text{elastic}} = {} & \eta\left[{}^m c_{ij}^M\left(\varepsilon_i - \varepsilon_i^0\right)\left(\varepsilon_j - \varepsilon_j^0\right)\right] \\ & + (1-\eta)\left[{}^e c_{ij}^P\left(\varepsilon_i - \varepsilon_i^0\right)\left(\varepsilon_j - \varepsilon_j^0\right)\right], \end{aligned} \tag{8}$$

where summation conventions over $i,j,k,l = 1,2,3$ (or $i,j,k,l = 1-6$ where a Voigt notation is adopted) are employed. $\boldsymbol{\mu}_r^\sigma$, $\boldsymbol{\kappa}_r^\sigma$, $\mathbf{c}^M$, and $\mathbf{c}^P$ are the stress-free relative magnetic permeability, stress-free relative dielectric permittivity, constant magnetization elastic stiffness, and constant polarization elastic stiffness, given by ${}^m\mu^\sigma_{rij} = {}^m\mu_{rij} + {}^m q_{ik}\,{}^m q_{jl}\,{}^m s_{kl}$, ${}^e\kappa^\sigma_{rij} = {}^e\kappa_{rij} + {}^e e_{ik}\,{}^e e_{jl}\,{}^e s_{kl}$, ${}^m c_{ij}^M = {}^m c_{ij} + {}^m q_{ki}\,{}^m q_{kj}/[\mu_0({}^m\mu^\sigma_{rkk} - 1)]$, and ${}^e c_{ij}^P = {}^e c_{ij} + {}^e e_{ki}\,{}^e e_{kj}/[\kappa_0({}^e\kappa^\sigma_{rkk} - 1)]$, respectively. $\mathbf{s}$ $(=\mathbf{c}^{-1})$ is the elastic compliance tensor. $\mathbf{H}^{\text{ext}}$, $\mathbf{H}^d$, $\mathbf{E}^{\text{ext}}$, and $\mathbf{E}^d$ are the external magnetic, demagnetization, external electric, and depolarization fields, respectively. ε^0 is the stress-free or phase transformation strain, which can be calculated as

$$\varepsilon_i^0 = \eta\frac{{}^m s_{ij}^M\,{}^m q_{kj} M_k}{{}^m\mu_{rkk} - 1} + (1-\eta)\frac{{}^e s_{ij}^P\,{}^e e_{kj} P_k}{\kappa_0({}^e\kappa_{rkk} - 1)}. \tag{9}$$

The demagnetization field $\mathbf{H}^d$ and the depolarization field $\mathbf{E}^d$ for the given distributions of magnetization and polarization are calculated by numerically solving the magnetostatic and electrostatic equations under periodic boundary conditions, i.e.,

$$\begin{cases} \partial H_i/\partial x_i = -\partial M_i/\partial x_i \\ \partial E_i/\partial x_i = -(1/\kappa_0)\cdot\partial P_i/\partial x_i, \end{cases} \tag{10}$$

where x_i is the ith component of the position vector in the Cartesian coordinates. The solution for Eq. (10) is obtained by introducing the magnetic scalar potential and electric potential, which are solved in the Fourier space; the details

are given in Refs. 38 and 39. The elastic field is obtained by solving the mechanical equilibrium equations

$$\partial c_{ijkl}\left(\varepsilon_{kl} - \varepsilon_{kl}^{0}\right)/\partial x_j = 0, \tag{11}$$

using an iteration method developed for materials with elastic inhomogeneity[40,41] based on Khachaturyan's microelasticity theory.[42] Note that a 3×3 strain tensor ε_{kl} is used in Eq. (11), while the Voigt notation is adopted elsewhere for simplicity. A clamped elastic boundary condition is employed, i.e., no macroscopic shape deformation happens for the composite materials during evolution.

The basic building block of the ME composites [see Fig. 1(a)] is discretized into a three-dimensional array of cubic grid cells, i.e., $n_1\Delta l \times n_2\Delta l \times n_3\Delta l$, where n_1, n_2, and n_3 denote the numbers of grid cells along the x_1, x_2, and x_3 axes, respectively, with a total grid cell number of around $n_1n_2n_3 = 300\,000$; Δl is the size of each grid in the real space. By properly choosing the grid numbers along each cubic axis and allocating the grid cells for BTO and CFO regions, systems with different aspect ratios r and phase fractions V_f of the CFO inclusions can be modeled. Δl is taken as 2.5 nm, corresponding to a total system size of $n_1\Delta l \times n_2\Delta l \times n_3\Delta l = 4\,500\,000$ nm^3. In this case, the lateral size of the CFO inclusions, e.g., $a = 28.2$ nm for $r = 100$ and $V_f = 0.5$, would be comparable to experiments (i.e., 20–30 nm, Ref. 43). Through solving Eq. (4) using the forward Euler method,[44] the magnetization and polarization distributions responsive to a given external field are obtained, and the effective direct ME response of the composite can then be calculated upon local magnetization/polarization/strain fields achieving an equilibrium.

Figures 2(a)–2(c) show the equilibrium spatial distributions of the local strain and polarization fields in the 0-3 type, 2-2 type, and 1-3 type CFO-BTO composites, respectively, in response to an external magnetic field along the positive x_3 axis, i.e., $H_3^{ext} = 100$ A/m. The volume fraction of the CFO phase V_f is fixed at 0.5. Upon this field, the magnetic CFO phase would expand in the x_1-x_2 plane [see the strain distributions of $\varepsilon_2(=\varepsilon_1)$ on the left of Figs. 2(a)–2(c)] due to its positive piezomagnetic coefficient $q_{32}(=q_{31})$, which leads to a compression near the contact region of the ferroelectric BTO phase in the lateral direction (denoted as region 1), i.e., a negative strain ε_2 $(=\varepsilon_1)$, due to zero shape deformation in the whole composite under the clamped elastic boundary condition. Accordingly, such in-plane compressive strains in the BTO phase induce a positive longitudinal polarization P_3 due to its negative piezoelectric coefficient $e_{32}(=e_{31})$ [see the polarization distributions on the right of Figs. 2(a)–2(c)]. Furthermore, CFO also expands along the longitudinal x_3 direction [see the strain distributions of ε_3 in the middle of Figs. 2(a)–2(c)] upon the positive H_3^{ext} because of a positive q_{33}. It compresses its intimately contacted BTO phase region in the longitudinal direction (denoted as region 2), i.e., a negative ε_3, and thus induces a negative P_3 in region 2 as $e_{33} > 0$.

Hence, the average polarization response $\overline{P_3}$ of the composite is determined by the competition between the lateral and longitudinal regions. For the laminated 2-2 type composites with a small r [see Fig. 2(b) for the case of $r = 0.02$], the BTO phase is dominated in volume by the longitudinal region 2, leading to an overall negative $\overline{P_3}$ as discussed above. However, the magnitude of $\overline{P_3}$ is small in such laminate geometry due to the strong longitudinal depolarization and demagnetization effect [Eq. (10)]. For 0-3 type composites [see Fig. 2(a) for the case of $r = 1$], the BTO phase is composed of region 1 and region 2 with comparable volumes. However, the contribution from the lateral region 1 is dominant due to the stronger depolarization in the longitudinal region 2, and therefore, the composite exhibits a positive $\overline{P_3}$. It also shows a larger magnitude than that in laminated composites due to the enhanced value of both the strain ε_2 and ε_3 (Fig. 2(a)) from the reduced longitudinal demagnetization (and therefore a larger M_3) in such particulate ME composites. Finally, in the 1-3 type ME composites with an even larger aspect ratio r [=10 in Fig. 2(c)] for the CFO rod, the volume of the lateral region 1 becomes dominant, leading to a positive $\overline{P_3}$. The greatly reduced longitudinal depolarization and demagnetization effects in such vertical geometry further enhance the magnitude of this positive $\overline{P_3}$, indicating a very strong ME coupling.

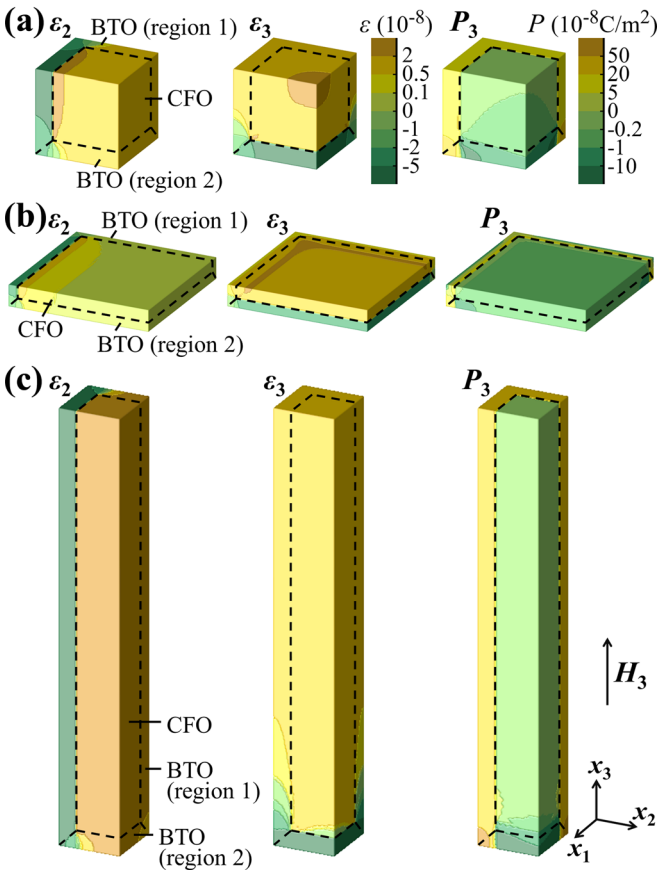

FIG. 2. Equilibrium distributions of the lateral strain ε_2, longitudinal strain ε_3, and the longitudinal polarization P_3 responsive to a longitudinally applied magnetic field $H_3 = 100$ A/m, in composites of (a) 0-3 ($r = 1$), (b) 2-2 ($r = 0.02$), and (c) 1-3 ($r = 10$) connectivities, with the CFO phase fraction V_f taken as 0.5. For clarity, only 1/8 (half length in each dimension) of one building block is shown. Dashed lines indicate the CFO/BTO phase boundaries and the partition of lateral and longitudinal regions in the BTO phase.

With these magnetic-field-induced polarization distributions in mind, the effective direct ME coefficient α_{ij} (in the unit of s/m) can be easily calculated following the constitutive equations (Eq. (3)), expressed as

$$\alpha_{ij} = \overline{P_i}/H_j^{ext}. \tag{12}$$

For illustration, Figure 3(a) presents the effective ME coefficient α_{33} of CFO-BTO composites with a fixed CFO phase fraction $V_f = 0.5$ as a function of the aspect ratio r. The composite shows a small and negative α_{33} at a low r below 0.05 (2-2 type). As aspect ratio increases, α_{33} undergoes a sign change and then increases significantly at $r > 1$, indicating a reversal of the net longitudinal polarization $\overline{P_3}$ from downward to upward direction as discussed above.

Moreover, the effective ME voltage coefficient α_{E33} (in the unit of $\mathrm{mV\,cm^{-1}\,Oe^{-1}}$) can be written as $\alpha_{E33} = -\alpha_{33}/(\kappa_0\kappa_{r33})$. The relative dielectric permittivity $\boldsymbol{\kappa}_r$ of the composite can be calculated following Eq. (3) with the equilibrium average electric displacement $\overline{\mathbf{D}}$ obtained under an applied external electric field $\mathbf{E}^{\mathrm{ext}}$

$$\kappa_{rij} = \overline{D_i}/\left(\kappa_0 E_j^{\mathrm{ext}}\right). \tag{13}$$

We employ a small electric field $E_3^{\mathrm{ext}} = 50\,\mathrm{V/cm}$ along the positive x_3 axis. Dependences of the effective α_{E33} and κ_{r33} on the aspect ratio r are shown in Fig. 3(b) and its inset, respectively. As seen, the composite shows a dielectric permittivity starting from a small $\kappa_{r33} = 48$ for $r = 0.01$. The dielectric constant is greatly enhanced with an increasing r to a large $\kappa_{r33} = 682$ for $r = 200$, which can be explained in the context of an equivalent serial circuit of the low-capacitance CFO and the high-capacitance BTO for the 2-2 laminated geometry gradually changing to an equivalent parallel circuit for the 1-3 rod geometry. As a combined property of α_{33} and κ_{r33}, the ME voltage coefficient α_{E33} is positive in the laminated composites ($r < 0.05$), undergoes a sign change at around $r = 0.05$ (belonging to 0-3 particulate composites), and then increases remarkably on increasing r in 0-3 ($0.05 \le r < 10$) particulate and 1-3 ($r \ge 10$) rod composites.

Besides the ME response, the piezoelectric and piezomagnetic properties of the composite can also be obtained by examining the induced average polarization and magnetization upon imposing a uniaxial net strain $\overline{\varepsilon_j}$ (taken as 0.01% herein), i.e., $e_{ij} = \overline{P_i}/\overline{\varepsilon_j}$ and $q_{ij} = \mu_0\overline{M_i}/\overline{\varepsilon_j}$. Shown in Figs. 3(c) and 3(d) are the variations of the longitudinal piezoelectric coefficient e_{3i} ($i = 1, 3$) and piezomagnetic coefficient q_{3i} ($i = 1, 3$) with the aspect ratio r. Both coefficients gradually increase with an increasing r, indicating a higher longitudinal piezoelectric and piezomagnetic coupling in the 1-3 rod composites, which would allow a stronger elastic interaction across the CFO/BTO interface and hence a larger direct ME effect. By contrast, the average longitudinal polarization $\overline{P_3}$ and magnetization $\overline{M_3}$ in the 2-2 laminated composites would be suppressed by large longitudinal depolarization and demagnetization fields, respectively, leading to smaller piezoelectric and piezomagnetic coefficients and a weaker direct ME coupling.

We further study the influence of the phase fraction V_f on the direct ME coefficient, as shown in Fig. 4(a). The obtained results agree well with previous predictions based on Green's function approach[6] in CFO-BTO composites with ellipsoidal CFO inclusions. As can be seen, for all aspect ratios studied, the direct ME coefficient α_{33}, which is zero in the single CFO and BTO phases (i.e., $V_f = 1$ and 0), emerges in the composite and reaches a maximum at a certain phase fraction. For instance, the maximum value of α_{33} at $r = 100$ is about 2.81×10^{-9} s/m at $V_f \approx 0.59$ (Fig. 4(a)). To better understand this, the elastic interaction between the BTO and CFO phases is examined. For the clamped case studied, the average field-induced strain in the CFO and BTO phases, i.e., $\overline{{}^m\boldsymbol{\varepsilon}}$ and $\overline{{}^e\boldsymbol{\varepsilon}}$, would be related as $V_f\overline{{}^m\boldsymbol{\varepsilon}} = -(1 - V_f)\overline{{}^e\boldsymbol{\varepsilon}}$, where $V_f\overline{{}^m\boldsymbol{\varepsilon}}$ could be considered as the average strain transferred across the CFO/BTO interface, i.e., the strength of the elastic interaction. As an example, Figure 4(b) shows the $V_f\overline{{}^m\boldsymbol{\varepsilon}}$ as a function of V_f in composites with different aspect ratios r. The maximum $V_f\overline{{}^m\varepsilon_1}$ appears at medium phase fractions (e.g., $V_f \approx 0.59$ for $r = 100$), where both $\overline{{}^m\boldsymbol{\varepsilon}}$ and $\overline{{}^e\boldsymbol{\varepsilon}}$ can reach a relatively large value and hence ensure the largest ME coupling coefficient α_{33} (Fig. 4(a)).

It is also worth noting that the phase fraction V_f for the maximum α_{33} gradually shifts towards the CFO-rich side (i.e., $V_f > 0.5$) from 0.59 to 0.74 as the aspect ratio r

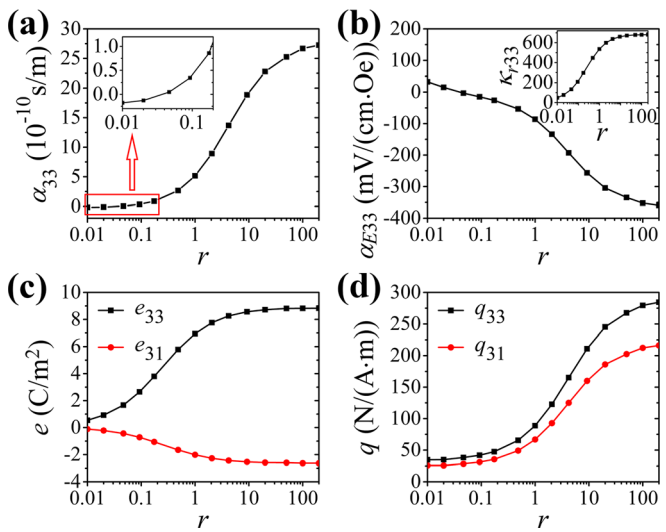

FIG. 3. Effective (a) ME coefficients (enlarged scale of the red rectangle part shown as inset), (b) ME voltage coefficients (relative dielectric permittivity shown as inset), (c) piezoelectric coefficients, and (d) piezomagnetic coefficients of the CFO-BTO composites as a function of the aspect ratio r. The volume fraction of the CFO phase is set to be 0.5.

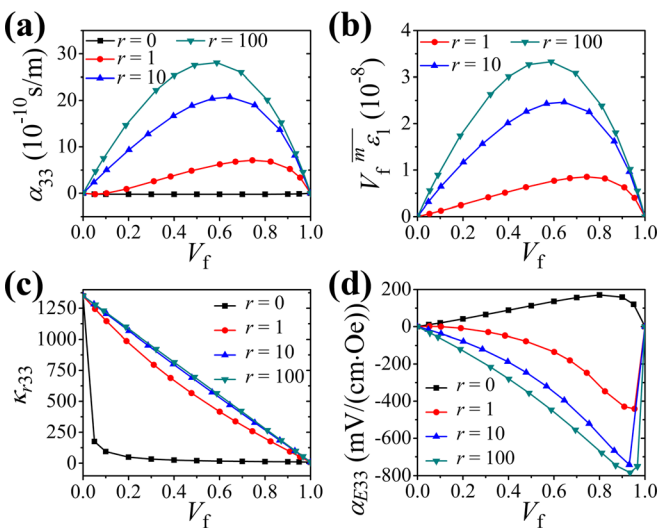

FIG. 4. Effective (a) ME coefficients, (c) relative dielectric permittivity, and (d) ME voltage coefficients of the CFO-BTO composite with different aspect ratios r as a function of the phase-fraction V_f. (b) $V_f\overline{{}^m\varepsilon_1}$ of the composite with different aspect ratios r upon applying a magnetic field $H_3^{\mathrm{ext}} = 100\,\mathrm{A/m}$, as a function of the phase-fraction V_f.

decreases from 100 to 1 [see Fig. 4(a)]. This is because higher volume fractions V_f would be required to compensate the shrinking area of contact interface in the cases of 0-3 particulate composites compared to the relatively large interface area in the 1-3 rod composites, such that the transferred field-induced strain can remain at a high value.

On the other hand, the effective longitudinal dielectric constant κ_{r33} rapidly decreases with increasing CFO phase fraction V_f (Fig. 4(c)) due to the much smaller dielectric permittivity of the CFO while it demonstrates a V_f dependence characteristic of an equivalent serial circuit of the low-capacitance CFO and the high-capacitance BTO for the 2-2 type structure ($r = 0$) and of an equivalent parallel circuit for the 1-3 type structure ($r = 100$). Figure 4(d) shows the effective ME voltage coefficient α_{E33} as a function of CFO phase fraction V_f. As shown, the strongest ME voltage response emerges in heavily CFO-rich side where κ_{r33} is small. For example, the largest α_{E33} is obtained as $-783\,\mathrm{mV/(cm\,Oe)}$ at $V_f = 0.93$ and $r = 100$.

In summary, a phase-field model coupled with constitutive equations has been developed to investigate the direct ME coupling in bulk multiferroic magnetic-ferroelectric composites. It provides a detailed examination of the composites that go from the mesoscopic modeling of the local polarization/elastic field distributions (domains) to the predictions of effective magnetoelectric response within the context of the continuum media theory under a periodic boundary condition. These functional properties have proven to be strongly dependent on several microstructural factors of the composites, including the phase fraction and phase connectivity. Such a simple phase-field based multi-scale approach should also have broad potential applications in predicting various effective properties, such as the piezoelectric,[45] piezomagnetic,[46] dielectric,[47] and elastic[48] responses, in composite materials, which are directly deduced from the response of the complex microstructure to external fields. This model can also be extended to include non-linear contributions to the effective properties, e.g., from domain wall motion, by incorporating magnetic exchange energy[38] and ferroelectric gradient energy[25,49] in total free energy to describe magnetic and ferroelectric domain walls, respectively.

This work was supported by the National Science Foundation (Grant Nos. DMR-1006541 and DMR-0820404) and the NSF of China (Grant Nos. 51332001, 51221291, and 11234005). The computer simulations were carried out on the LION and Cyberstar clusters at the Pennsylvania State University supported in part by NSF Major Research Instrumentation Program through Grant No. OCI-0821527 and in part by the Materials Simulation Center and the Graduated Education and Research Services at the Pennsylvania State University.

[1]M. Fiebig, J. Phys. D **38**, R123 (2005).
[2]W. Eerenstein, N. D. Mathur, and J. F. Scott, Nature **442**, 759 (2006).
[3]C. W. Nan, M. I. Bichurin, S. Dong, D. Viehland, and G. Srinivasan, J. Appl. Phys. **103**, 031101 (2008).
[4]C. A. F. Vaz, J. Hoffman, C. H. Ahn, and R. Ramesh, Adv. Mater. **22**, 2900 (2010).
[5]J. Ma, J. Hu, Z. Li, and C.-W. Nan, Adv. Mater. **23**, 1062 (2011); J.-M. Hu, J. Ma, J. Wang, Z. Li, Y. H. Lin, and C. W. Nan, J. Adv. Dielectr. **1**, 1 (2011).
[6]C. W. Nan, Phys. Rev. B **50**, 6082 (1994).
[7]C. Israel, N. D. Mathur, and J. F. Scott, Nature Mater. **7**, 93 (2008).
[8]E. Lage, C. Kirchhof, V. Hrkac, L. Kienle, R. Jahns, R. Knöchel, E. Quandt, and D. Meyners, Nature Mater. **11**, 523 (2012).
[9]T. Nan, Y. Hui, M. Rinaldi, and N. X. Sun, Sci. Rep. **3**, 1985 (2013).
[10]S. Dong, J. G. Bai, J. Zhai, J.-F. Li, G. Q. Lu, D. Viehland, S. Zhang, and T. R. Shrout, Appl. Phys. Lett. **86**, 182506 (2005).
[11]Y. Zhang, Z. Li, C. Y. Deng, J. Ma, Y. H. Lin, and C. W. Nan, Appl. Phys. Lett. **92**, 152510 (2008).
[12]X. Bai, Y. Wen, J. Yang, P. Li, J. Qiu, and Y. Zhu, J. Appl. Phys. **111**, 07A938 (2012).
[13]G. Harshe, J. P. Dougherty, and R. E. Newnham, Int. J. Appl. Electromagn. Mater. **4**, 145 (1993).
[14]C. W. Nan and D. R. Clarke, J. Am. Ceram. Soc. **80**, 1333 (1997).
[15]C. W. Nan, G. Liu, Y. Lin, and H. Chen, Phys. Rev. Lett. **94**, 197203 (2005).
[16]Y. Benveniste, Phys. Rev. B **51**, 16424 (1995).
[17]J. H. Huang and W. S. Kuo, J. Appl. Phys. **81**, 1378 (1997).
[18]J. Y. Li, Int. J. Eng. Sci. **38**, 1993 (2000).
[19]G. Liu, C. W. Nan, Z. K. Xu, and H. D. Chen, J. Phys. D: Appl. Phys. **38**, 2321 (2005).
[20]G. Liu, C. W. Nan, and J. Sun, Acta Mater. **54**, 917 (2006).
[21]T. Wu, M. A. Zurbuchen, S. Saha, R. V. Wang, S. K. Streiffer, and J. F. Mitchell, Phys. Rev. B **73**, 134416 (2006).
[22]N. A. Pertsev, H. Kohlstedt, and B. Dkhil, Phys. Rev. B **80**, 054102 (2009).
[23]V. G. Kukhar, N. A. Pertsev, and A. L. Kholkin, Nanotechnology **21**, 265701 (2010).
[24]L. Q. Chen, Annu. Rev. Mater. Res. **32**, 113 (2002).
[25]L. Q. Chen, J. Am. Ceram. Soc. **91**, 1835 (2008).
[26]J.-M. Hu, G. Sheng, J. X. Zhang, C. W. Nan, and L. Q. Chen, Appl. Phys. Lett. **98**, 112505 (2011).
[27]J.-M. Hu, G. Sheng, J. X. Zhang, C. W. Nan, and L. Q. Chen, J. Appl. Phys. **109**, 123917 (2011).
[28]J. X. Zhang, Y. L. Li, D. G. Schlom, L. Q. Chen, F. Zavaliche, R. Ramesh, and Q. X. Jia, Appl. Phys. Lett. **90**, 052909 (2007).
[29]Y. Ni and A. G. Khachaturyan, J. Appl. Phys. **102**, 113506 (2007).
[30]Y. Ni, L. He, and A. G. Khachaturyan, J. Appl. Phys. **108**, 023504 (2010).
[31]P. P. Wu, X. Q. Ma, J. X. Zhang, and L. Q. Chen, Philos. Mag. **90**, 125–140 (2010).
[32]R. E. Newnham, D. P. Skinner, and L. E. Cross, Mater. Res. Bull. **13**, 525 (1978).
[33]For $CoFe_2O_4$, $c_{11} = 286.0$GPa, $c_{12} = 173.0$GPa, $c_{33} = 269.5$GPa, $c_{13} = 170.5$GPa, $c_{44} = 45.3$GPa, $\mu_{r33} = 125$, $q_{31} = 580.3\mathrm{N/(Am)}$, $q_{33} = 699.7\mathrm{N/(Am)}$, and $\kappa_{r33} = 10$; for $BaTiO_3$, $c_{11} = 166.2$GPa, $c_{12} = 76.5$GPa, $c_{33} = 161.4$GPa, $c_{13} = 77.4$GPa, $c_{44} = 43.0$GPa, $\mu_{r33} = 8$, $\kappa_{r33} = 1350$, $e_{31} = -4.22\mathrm{C/m^2}$, and $e_{33} = 18.6\mathrm{C/m^2}$.
[34]C. W. Nan, Prog. Mater. Sci. **37**, 1 (1993).
[35]D. E. Gray, *American Institute of Physics Handbook*, 3rd ed. (Mcgraw Hill, New York, 1987).
[36]K. H. Hellwege, *Landolt-Börnstein Numerical Data and Functional Relationship in Science and Technology, New Series* (Springer, Berlin, 1978).
[37]S. M. Allen and J. W. Cahn, J. Phys. (Paris) **38**, C7 (1977).
[38]J. X. Zhang and L. Q. Chen, Acta Mater. **53**, 2845 (2005).
[39]Y. L. Li, S. Y. Hu, Z. K. Liu, and L. Q. Chen, Appl. Phys. Lett. **81**, 427 (2002).
[40]S. Y. Hu and L. Q. Chen, Acta Mater. **49**, 1879 (2001).
[41]P. Yu, S. Y. Hu, L. Q. Chen, and Q. Du, J. Comput. Phys. **208**, 34 (2005).
[42]A. G. Khachaturyan, *Theory of Structural Transformation in Solids* (Wiley, New York, 1983).
[43]H. Zheng, J. Wang, S. E. Lofland, Z. Ma, L. Mohaddes-Ardabili, T. Zhao, L. Salamanca-Riba, S. R. Shinde, S. B. Ogale, F. Bai *et al.*, Science **303**, 661 (2004).
[44]W. H. Press, B. P. Flannery, S. A. Teukolsky, and W. T. Vetterling, *Numerical Recipes in Fortran 77: The Art of Scientific Computing*, 2nd ed. (Cambridge University Press, Cambridge, 1992), p. 710.
[45]W. Liu and X. Ren, Phys. Rev. Lett. **103**, 257602 (2009).
[46]S. Yang, H. Bao, C. Zhou, Y. Wang, X. Ren, Y. Matsushita, Y. Katsuya, M. Tanaka, K. Kobayashi, X. Song, and J. Gao, Phys. Rev. Lett. **104**, 197201 (2010).
[47]Y. U. Wang, Appl. Phys. Lett. **96**, 232901 (2010); J. Appl. Phys. **110**, 044103 (2011).
[48]S. Bhattacharyya, T. W. Heo, K. Chang, and L. Q. Chen, Modell. Simul. Mater. Sci. Eng. **19**, 035002 (2011).
[49]Y. L. Li, S. Y. Hu, Z. K. Liu, and L. Q. Chen, Appl. Phys. Lett. **78**, 3878 (2001).